



Evaluating the impact of the building density and height on the block surface temperature



Yunhao Chen^{a,b}, Jiatong Wu^c, Ke Yu^{a,b,*}, Dandan Wang^{a,b}

^a Faculty of Geographical Science, State Key Laboratory of Earth Surface Processes and Resource Ecology, Beijing Normal University, Beijing, 100875, China

^b Beijing Key Laboratory of Environmental Remote Sensing and Digital Cities, Beijing Normal University, Beijing, 100875, China

^c Map Supervision Center of Ministry of Natural Resources, Beijing, 100830, China

ARTICLE INFO

Keywords:

Urban geometry
Surface temperature
ENVI-met
Floor area ratio

ABSTRACT

Urban surface structures affect block surface temperatures, thermal loading of pedestrians, wind patterns and more. Comparisons of the building density and height impact on block surface temperature and optimization at a fixed floor area ratio (FAR) are rare. In this research, a 3-dimensional simulation model, ENVI-met, is used to simulate block surface temperature in different scenarios and evaluate the urban geometry impact on surface temperature of each component (roof, street and four-oriented walls). Results show that: (1) the increased building density (λ_p) and height (H) cool blocks at unfixed FARs; (2) buildings with λ_p and H of 0.36 and 10 m with a fixed FAR of 1.5 produce the highest summer surface temperatures for all studied components; (3) when FAR is fixed, among scenarios with $\lambda_p \leq 0.36$ and $H \geq 10$ m, building height dominates component surface temperature by reducing the solar radiation reaching the surface. Among scenarios with $\lambda_p > 0.36$ and $H < 10$ m, building density becomes more important in reducing heat loss; (4) the lower parts of western and eastern walls on summer and winter days and of southern walls on winter days are cooler because more shadows cast onto walls, whereas the lower parts of northern walls over the two days and of southern walls on summer days are warmer because walls absorb more ground radiation with high-rise and low-density buildings. This study can provide instructions for urban design in mitigating the urban heat impact on human health and decreasing building energy requirements.

1. Introduction

With the rapid development of cities over the last half century, the expansion of artificial structures increases surface thermal storage capacity and the solar radiation absorbed by the earth surface and changes the heat exchange between surfaces and the atmosphere [1]. Such changes aggravate the urban heat island (UHI) effect and lead to deterioration of the urban thermal environment, posing a threat to human health [2–5]. Many improvements in the urban thermal environment focusing on parameters such as surface temperature, absorbed radiation and wind speed include optimizing urban geometries and utilizing natural surfaces (vegetation, water bodies and parks) and other reflective surfaces (cool pavements and green roofs) [4–7]. Among these improvements, the influence of urban geometry lies in changing the land surface shortwave absorption and longwave emission and heat exchange patterns near the ground and forming local microclimates [8–10]. Buildings act as obstacles by reducing wind speed and altering heat

convection [11], and a denser building arrangement could store more energy by decreasing sky openness, further deteriorating the urban thermal environment [12]. Moreover, a three-dimensional (3-D) urban surface structure creates sunlit and shaded patterns on each surface component (i.e., roofs, ground or walls) with differential surface heating, resulting in pronounced microscale temperature variation [13,14]. Clearly, microscale block geometry studies can better present the interactions between building geometry and thermal environment parameters, which has become a major concern compared with the inevitable urban spatial heterogeneity and urban-scale missing 3-D building information, particularly the rapidly developing thermal remote sensing methods [15–18].

At the block scale (residential, commercial districts, campuses and streets), the building geometry could be described by the sky view factor (SVF) and height-to-width ratio (H/W) related to building density and height and street orientation [19,20]. Various researchers focus on the correlation between these three parameters and radiance, wind speed,

* Corresponding author. , Faculty of Geographical Science, Beijing Normal University, No. 19, XinJieKouWai St., HaiDian District, Beijing, 100875, China.
E-mail addresses: cyh@bnu.edu.cn (Y. Chen), wjt20111001234@163.com (J. Wu), yuke25@mail.bnu.edu.cn (K. Yu), rswdd@mail.bnu.edu.cn (D. Wang).

and air temperature or thermal comfort. For instance, larger SVF could decrease the daytime air temperature and increase the nighttime air temperature, wind speed and time-averaged physiologically equivalent temperature (PET) at local scales [21–23]. Furthermore, the SVF could be a predictor of the solar irradiation on building facades for the latitudes from 38° to 60° [24]. Chatzidimitriou et al. discovered that the mean radiant temperature differences could reach 22 K and 4 K due to street orientation and H/W ratio variations, respectively, in summer [25]. Andreou found that the PET level never enters the comfort zone for H/W ratios from 0.6 to 2.0 on E-W streets, while the best comfort condition occurs on N-S streets for H/W ratios from 0.8 to 1.3 [26]. Relevant analysis could also be found in Refs. [27–31].

The above studies mainly use two methods for parameter acquisition and quantitative assessment of the impact of building geometry on the block thermal environment including field measurements and model simulation. The former uses fixed stations and mobile sensors to monitor meteorological and urban geometry parameters. Infrared cameras, radiometers, ultrasonic anemometers and fish-eye lens photography are typically used [32–35]. Unfortunately, the high resource costs and lack of spatiotemporal continuous observations in neighborhoods of different geometries make it difficult to conduct analysis using field measurements [36]. Moreover, previous studies have revealed that fluctuations in atmospheric and field conditions, seasons and equipment errors may reduce the reliability of the experimental results [37]. Due to the complexity of the block thermal environment, numerical or computer simulations have become important tools to study the microclimate environments of neighborhoods in recent years. Various models successfully simulated real microscale block scenarios, particularly energy balance models (EBMs) and computational fluid dynamics (CFD) [38]. However, in the existing model simulation studies, deficiencies still exist. First, most of the studies did not consider the urban carrying capacity. Studying the impacts of building geometry parameters (represented by building density and height) separately is not enough to provide city or neighborhood design suggestions that should be able to accommodate a sufficient population. Therefore, controlling the building capacity within a reasonable range and further studying the block thermal environments related to building geometries are more meaningful for improving of urban thermal environments [39,40]. Second, most previous studies analyzed block thermal environment parameters based on two-dimensional surfaces, while 3-D component surface temperature distribution analysis is rare, especially of vertical walls of different orientations with significant vertical heterogeneities that notably affect air convection and heat exchange. Third, the building geometry impact on the nighttime block energy balance is neglected. The differential performance of block surface temperatures in different seasons has not received much attention. For example, a CFD simulation (URANS) successfully simulated the air temperature, surface temperature and wind speed of dense highly heterogeneous districts in Nicosia, Cyprus, in summer, but winter results are still lacking [41].

In our study, the floor area ratio (FAR) is used to indicate a neighborhood's carrying capacity. The FAR is defined as the ratio of the total construction space to the land area and can be calculated by multiplying the building height and density [42]. Numerical urban microclimate software ENVI-met is used to simulate block surface temperature in different building geometry scenarios [43]. We analyze impact of building geometry on daytime and nighttime component surface temperature (i.e., roofs, streets and four oriented walls) on summer and winter days for different building densities and heights and different building density and height combinations under a fixed FAR and further compare the differences caused by limiting FAR. The heterogeneity of wall surface temperature distribution in the vertical dimension is also necessarily examined.

In this paper, section 2 introduces ENVI-met and software evaluation using field measurements. Section 3 describes the scenario design details of the three experiments and research methods in our study. In section 4, we analyze the impact of building height and density and the combined

effect under a fixed FAR on the surface temperature of each component. Section 5 provides deeper discussions on both the temporal variations and the heterogeneity of wall surface temperature in the vertical dimension for the different building density and height combinations under a fixed FAR and section 6 concludes the study.

2. Model description and evaluation

2.1. ENVI-met

ENVI-met is a 3-D microclimate model designed to simulate the interactions between buildings, ground, vegetation, soil and atmosphere in urban environments based on the fundamental laws of fluid dynamics and thermodynamics relying on the Reynolds-Averaged Navier-Stokes (RANS) equation to obtain urban airflow and heat transfer patterns [44]. The mathematical model of ENVI-met is mainly divided into six parts, including the atmospheric model (wind field, air temperature, humidity and turbulence simulation), radiation model, soil model, vegetation model, building model and surface EBMs. A detailed description about these models can be seen in Bruse [43]. In ENVI-met, the simulation resolution can be down to 0.5 m in space and 1–5 s in time. The high resolution allows for fewer spatial and temporal discontinuities of the simulated surface temperature over the course of a day. The latest version (ENVI-met V 4.0) includes thermal mass and heat inertia as building model settings and provides user-definable background meteorological conditions to set hourly air temperatures and humidities based on measured meteorological data [45].

As one of the most popular dynamic simulation tools, the easy operation, friendly user interface and comprehensive simulation systems have exponentially increased the number of publications applying ENVI-met for urban microclimate research from 1998 to 2017, which has demonstrated the superior simulation accuracy and feasibility of ENVI-met [36,46–50]. The focus of our research is the simulation of surface temperature (streets and buildings), and the new version of ENVI-met (V 4.0) was used.

2.2. Model evaluation

In this section, the simulated road, building and grassland surface temperatures were compared with the field measurements to evaluate the accuracy of ENVI-met simulated surface temperature. For ease of discussion, this is called the field experiment.

2.2.1. Field measurements and model settings

A field experiment was conducted at the Fangshan Experimental Base of Beijing Normal University from 6:00 a.m. on July 12 to 6:00 a.m. on July 13, 2017. The field is located at 116°03'18.3"E and 39°41'29.1"N and cover an area of 37800 m². A landscape overview is shown in Fig. 1(a). Five infrared temperature measurement systems (BODACH SUP03; spectral range: 8–14 μm; measurement range: -20 to 100 °C; accuracy: ±1%) were used to collect temperature data of the roof and four walls of a building. The building is surrounded by a relatively flat area consisting of short grass, soil, and concrete. The walls of the buildings are covered by red clay, and the roof is covered by concrete. The radiometers were placed at a height of 1.75 m and a distance of 50 cm from each wall surface. The infrared probe angle was 45° upward. The building is constructed in the north-south direction with no other buildings nearby. Therefore, there are no shadows cast on the walls by adjacent buildings, and the measured point temperatures by the fixed radiometers are more representative for model evaluation. A thermal infrared imager (Fluke IR-FlexCam 8800; spectral range: 8–14 μm; measurement range: -20 to 1200 °C; accuracy: ±2%) was used to measure the grassland and concrete surface temperature distributions. Data were sampled at an interval of 15 min. The weather is clear with small clouds at approximately 13:00. A hand-held laser distance meter (PD42; measurement range: 0.05–200 m; accuracy: ±1 mm) was

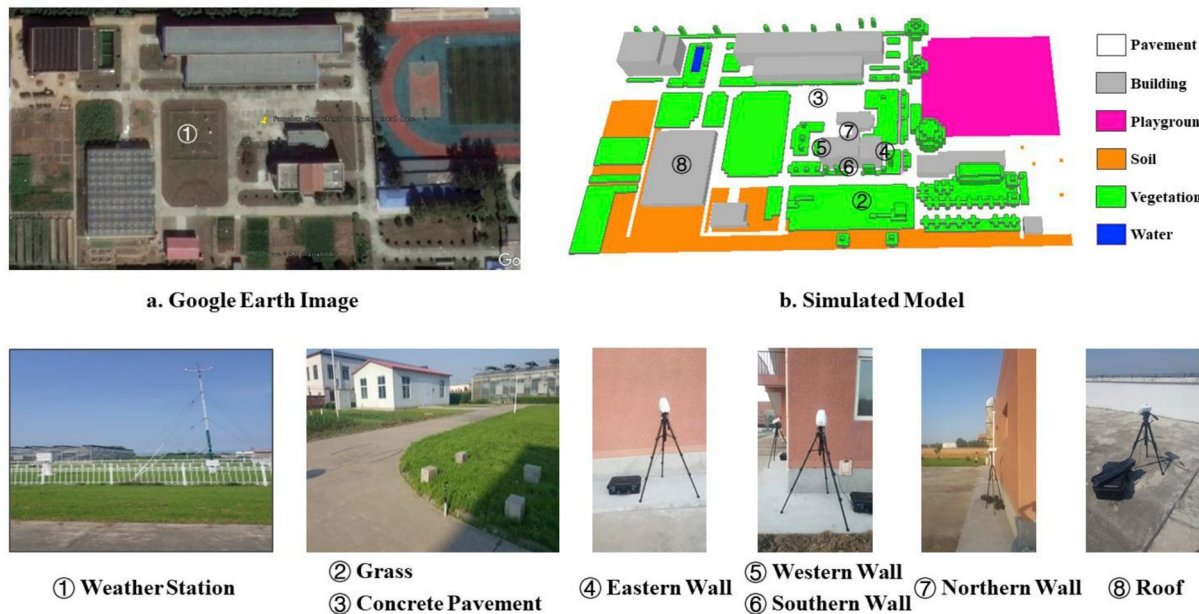


Fig. 1. Landscape overview of the experimental area and the simulated scene input into ENVI-met and instruments at each site.

used to measure the length, width and height of 7 buildings, 45 trees, and 7 bushes. The building, tree and bush heights in this area are between 6 m and 16 m, 3 m and 20 m, and 0.75 m and 1.2 m, respectively.

The simulation interval is consistent with the measurement interval, with a time step of 2 s. Considering that ENVI-met usually requires a long initialization period to obtain accurate simulation results, modeling lasts 27 h, but only the results of the last 24 h are used for analysis [45]. The modeling domain is $135 \times 70 \times 30$ (number of x, y, and z grids), and the grid resolution is set as $2 \text{ m} \times 2 \text{ m} \times 2 \text{ m}$. The building and vegetation heights were set according to the measurement results. To make the edge simulation results more accurate, five nested grids were set up around the experimental area [46]. The simulated scenario is shown in Fig. 1 (b). The initial wind speed and wind direction were set to 9 m/s

and 85° (counterclockwise from the north), respectively. The surface roughness was 0.01 m, and ENVI-met was run with no clouds. We used the default setting in ENVI-met for the thermoradiative parameters of the materials (see Table 1). Considering that the material of the plastic playground cannot be defined in ENVI-met, bricks with a higher reflectivity were used as an alternative. The atmospheric temperature and relative humidity were input at a time step of 1 h. Values of the two variables for the summer case are shown in Fig. 2. The meteorological parameters and the three-layer soil temperatures were collected from the weather station in Fangshan.

2.2.2. Evaluation results

The ENVI-met simulated component surface temperatures were

Table 1
Input thermoradiative parameters of the artificial and natural surfaces used in the ENVI-met simulations.

Materials		Surface Albedo	Emissivity	Thickness (m)	Volumetric Heat Capacity ($\text{J}\cdot\text{m}^{-3}\cdot\text{K}^{-1}$)	Heat Conductivity ($\text{W}\cdot\text{m}^{-1}\cdot\text{K}^{-1}$)	
Pavement	Concrete	0.50	0.90	0.25	2.08	0.86	
	Sand	-	0.90	0.05	1.46	0.27	
Street	Asphalt	0.20	0.90	0.25	2.25	0.90	
	Loam	0.20	0.98	0.05	1.21	0.75	
Playground	Basalt brick	0.80	0.90	0.06	2.39	1.73	
	Sand	-	0.93	0.02	1.46	0.27	
Materials		Reflectivity	Emissivity	Thickness (m)	Specific Heat Capacity ($\text{J}\cdot\text{kg}^{-3}\cdot\text{K}^{-1}$)	Heat Conductivity ($\text{W}\cdot\text{m}^{-1}\cdot\text{K}^{-1}$)	
Buildings	Concrete (hollow block)	0.30	0.91	0.30	840	0.86	
Materials		Surface Albedo	Emissivity	Volumetric heat capacity ($\text{J}\cdot\text{m}^{-3}\cdot\text{K}$)	Soil layer	Initial temperature (K)	
Soil	Loam	0.20	0.98	1.21	Upper layer (0-0.2 m) Medium layer (0.2-0.5 m) Deep layer (>0.5 m)	300.38 311.45 299.30	50 60 60
Grass (dense)	CO ₂ Fixation Type C3	Surface Albedo 0.20		Plant Height (m) 0.63	Root Zone Depth (m) 0.50	Leaf Area Density (LAD) 0.30	

Street is the ground material in the scenario experiments in section 3.1 in order to better match the urban street condition. All buildings in the field and scenario experiments are hollow concrete blocks.

(-) represents the surface albedo of sand materials were not provided in ENVI-met.

The materials of water and trees are not listed in Table 1 because they are not the focus of our research and the area is small.

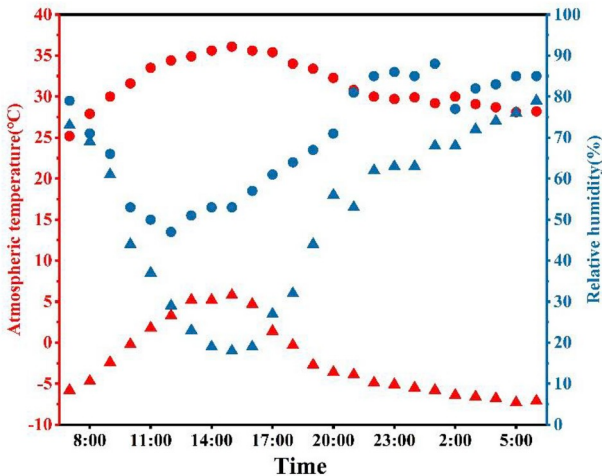


Fig. 2. The hourly atmospheric temperature and relative humidity input into ENVI-met. The red and blue circles are input atmospheric temperature and relative humidity respectively in the field experiment and scenario experiments on July 12; the red and blue triangles are input atmospheric temperature and relative humidity in the scenario experiments on November 12. The scenario experiments are in section 3.1. The datasets are collected from Fangshan weather station. (For interpretation of the references to colour in this figure legend, the reader is referred to the Web version of this article.)

compared to point measurements. As the most widely applied statistics, the root-mean-square error (RMSE), mean absolute error (MAE), mean bias error (MBE), the index of agreement d and the coefficient of determination R^2 were used to evaluate the accuracy of ENVI-met [45]. The detailed equations for these indexes are provided in Table A1 in Appendix 1. The evaluation results are shown in Table 2. The simulated and measured results are highly correlated with R^2 and d are larger than 0.98 and 0.95 for all cases respectively, except for grass. Moreover, RMSE, MAE and MBE are below 1.7°C for all components. The simulation accuracy of ENVI-met is a little lower over grass because it did not capture temperature heterogeneity over grass surfaces in the experiment area. However, our research focuses on the surface temperature of buildings whereas the vegetation model input was considered as a background value. Therefore, the validation results demonstrate that ENVI-met can be used as a tool to investigate the effect of urban geometry on urban surface temperatures.

3. Method

To analyze the impact of building geometry on component surface temperature, three experiments were designed to limit the building density, building height and FAR, respectively. Then the surface temperature was simulated both for daytime and nighttime. The scenario constructions are shown in Table 3. For ease of discussion, the three scenarios are named the density (low, medium and high densities), height (small, medium and large heights) and FAR (different densities and heights at a fixed FAR) experiments, respectively. Details about the experimental design are provided in section 3.1.

Table 2
Quantitative evaluation of ENVI-met model performance with measured data.

Component surface	R^2	RMSE($^\circ\text{C}$)	MAE($^\circ\text{C}$)	MBE($^\circ\text{C}$)	d
Eastern wall	0.991	1.181	1.073	-0.874	0.993
Western wall	0.982	1.110	0.919	0.075	0.995
Southern wall	0.981	1.618	1.411	-1.380	0.982
Northern wall	0.989	0.516	0.380	-0.339	0.995
Roof	0.987	1.313	1.133	-0.475	0.995
Ground	0.991	1.139	1.140	-0.113	0.990
Grass	0.883	1.414	1.166	0.513	0.965

3.1. Scenario design

The buildings in all simulated scenarios were designed with a north-to-south direction. The ratio of the total base area to the land area of all the buildings can directly reflect the building intensity of a certain area; hence, λ_p presents the building density [51]. For the density experiments, the building height was fixed at 15 m, whereas λ_p of 0.0625, 0.16, 0.25, 0.36, 0.49, and 0.64 were used. These density values were selected based on analysis results of the buildings in Beijing, where the density commonly ranges from 0.125 to 0.25 across the Beijing Five Rings, and the density is usually 0.0625 in the suburbs [51]. Considering the integrity of the study, scenarios with a higher building density, like density range of Hong Kong, were also included in our research [52]. For the height experiment, the building density was fixed at 0.25, whereas the building height was set to 7.5 m, 15 m, 30 m, 45 m and 60 m. The effect of different building density and height combinations on component surface temperatures under a fixed FAR was also analyzed. According to the calculation rule of Beijing Municipal Commission of Planning and Natural Resources [39], the standard FAR value in high-rise building areas is 1.5. The typical floor height in this area is 2.5 m according to the Chinese Ministry of Housing and Urban-Rural Development (<http://www.mohurd.gov.cn/>). The FAR is calculated as follows:

$$\text{FAR} = \frac{S_U}{A_L} = \frac{A_B \times N_f}{A_L} = \lambda_p \times N_f = \lambda_p \times H / F_H \quad (1)$$

where S_U , A_L , A_B , N_f and F_H are the total useable floor space, total land area, building base area, number of floors and floor height, respectively.

Therefore, different building density and height combinations at a fixed FAR according to formula (1) were designed to analyze the influence of these combinations on block surface temperatures in the FAR experiments.

3.2. Simulation of component surface temperatures

The detailed physical and thermoradiative properties of the street and buildings in the three ENVI-met experiments are summarized in Table 1. One day in summer (July 12, 2017) and one day in winter were selected due to more significant block surface temperature variations compared to those in spring and autumn. Finally, component surface temperatures in the three experiments were simulated for a 24-h period by ENVI-met from 6:00 a.m. to 6:00 a.m. of the next day for both the summer and winter cases. Referring to the field experiment in section 2.2.1, modeling lasts 27 h, but only the results of the last 24 h are used for analysis. The initial atmospheric forcing data in ENVI-met are listed in Table 4 and the hourly input atmospheric temperature and relative humidity are displayed in Fig. 2. The modeling domain is $60 \times 60 \times 35$ (number of x, y, and z grids), with a resolution of $2 \text{ m} \times 2 \text{ m} \times 3 \text{ m}$ in the x, y and z dimensions, respectively. Five nested grids (actual total space of $70 \times 70 \times 35$) were set up in the x, y dimensions around the simulation space to reduce the simulation errors at the scene edges.

The definition of each component is shown in Fig. 3. The integrated component surface temperatures (T_g , T_e , T_w , T_s , T_n and T_r) were defined to quantify the ability of a block surface to absorb and store solar radiation. In this research, the impact of building geometry on the integrated temperature on July 12 and November 12 is analyzed. The systematic simulated interval of ENVI-met is set to be 2 s in our study. Temperatures of grids of each block component surface were collected at 30-min intervals. The average temperature for each component is calculated as Eq. 2:

$$T_j = \frac{\sum_{i=1}^n \int_{t_1}^{t_2} T_i(t) dt}{n} \quad (2)$$

where j is the type of component; T_j is the mean temperature of component j ; n is the number of grids on each component; $T_i(t)$

Table 3
Urban canyon geometry design.

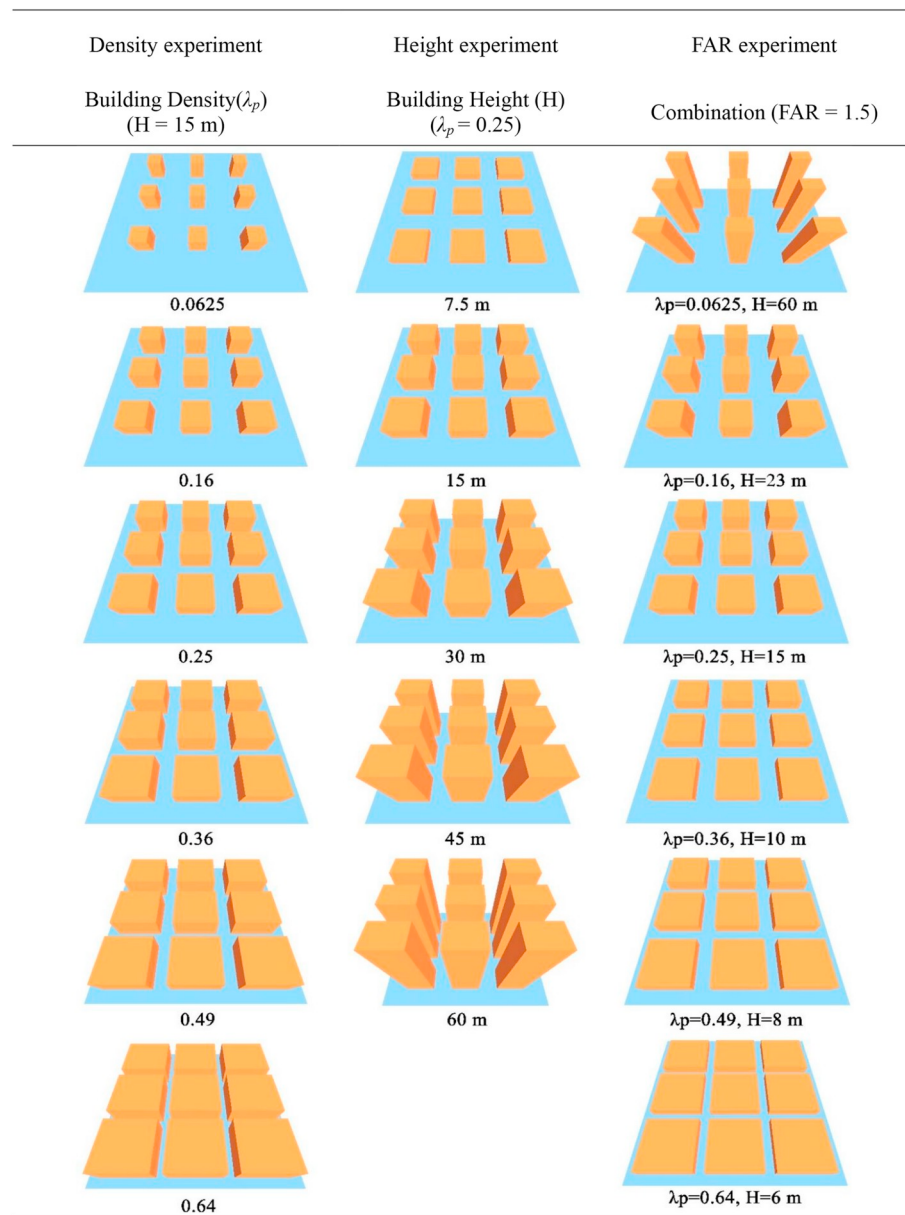


Table 4
Initial input meteorological parameters in ENVI-met for simulating component surface temperatures under different building geometries.

	July 12, 2017	November 12, 2017
Surface Roughness	0.01	0.01
Wind Speed (10 m height)	9 m/s	1.2 m/s
Wind Direction	85°	133°

represents the temperature of grid i at time t ; and t_1 and t_2 are the beginning and end of the simulation period.

According to the variation of simulated solar radiation in ENVI-met, the surface temperatures were integrated from 6:00 to 19:00 on July 12 and from 8:00 to 16:00 on November 12 as daytime integrated temperatures, while the remaining temperatures were combined as nighttime integrated temperatures.

To quantify the impact of building geometry on the integrated

component surface temperature, three indexes were used here including the daytime and nighttime integrated temperatures and the amplitude of temperature variation during a day which is calculated as the difference between the maximum and minimum temperatures. The daytime and nighttime integrated temperatures were separately analyzed to discuss the integrated temperature variation and their dominant factors with or without solar radiation in the three experiments, whereas the amplitude reflects the temperature fluctuation of each surface in time. These indicators are described in Ref. [37].

4. Results

4.1. The building density impact on block surface temperature (density experiment)

The T_g , T_e , T_w , T_s , T_n and T_r for different building densities are shown in Fig. 4. The six building density scenarios in Table 3 are called E1-1,

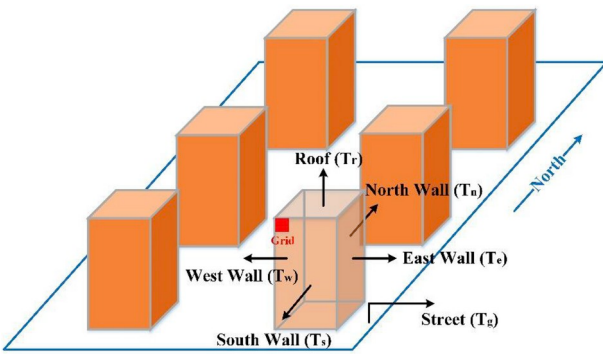


Fig. 3. Different component surfaces. T_g , T_e , T_w , T_s , T_n and T_r are the integrated temperatures of the street, eastern, western, southern and northern walls and roof, respectively. The red square is one grid on the wall surface. (For interpretation of the references to colour in this figure legend, the reader is referred to the Web version of this article.)

E1-2, E1-3, E1-4, E1-5 and E1-6.

In the daytime, T_g declines as λ_p increases because less solar radiation reaches the street surface, decreasing 74.67% and 73.43% from E1-1 to E1-6 over the two days, respectively. The impact of the increased building density on T_g is smaller on July 12 than on November 12 due to the stronger solar radiation and lower shadow ratio on the ground caused by the relatively higher sun elevation (70.92°) during the course of a summer day. As a result, the decrease in T_g initially is stable and then occurs fast from E1-3 to E1-6 on July 12 compared with November 12, and a similar amplitude variation trend is observed. The variation in T_g as λ_p increases shows a reverse pattern during the nighttime over the two days due to the reduced heat loss to the sky.

T_e , T_w , T_s and T_n all decrease as λ_p increases during the daytime due to the mutual shadowing between adjacent walls and less solar radiation reaching the wall's surface on July 12 and November 12. The integrated temperature reduction due to the decreasing solar radiation on daytime

with increasing λ_p is larger than the integrated temperature increase caused by the heat loss reduction on nighttime, so the nighttime integrated temperature on July 12 decreases for the four walls. The solar radiation is the powerful contributor of T_w and T_s because the western and southern walls experience the last sunlight before sunset. The increased λ_p leads to less daytime solar radiation being absorbed by the two walls and lower winter nighttime T_w and T_s . As λ_p increases, the integrated temperature reduction caused by the solar radiation reduction does not exceed the integrated temperature increase caused by the heat loss reduction. As a result, the nighttime T_e and T_n on November 12 increase with λ_p . The northern wall temperature amplitude over the two days increase reveals that a stronger reflectance in a more compact block occurs if not receiving direct solar radiation when other walls have weak, decreasing or stable amplitude trends.

In the summer and winter, the weak variation in daytime and nighttime T_r and amplitudes from E1-1 to E1-3 reveals that T_r is mainly controlled by solar radiation when λ_p is smaller than 0.25. The gradual decline in daytime T_r and amplitudes (from E1-3 to E1-6) is caused by the reduced upward block radiance with increasing λ_p .

4.2. The building height impact on block surface temperature (height experiment)

The block component surface temperature characteristics for different building heights with the same λ_p ($\lambda_p = 0.25$) are described in this section. The behavior of T_g , T_e , T_w , T_s , T_n and T_r and their temperature amplitudes for different building heights is shown in Fig. 5. The five building height scenarios in Table 3 are E2-1, E2-2, E2-3, E2-4 and E2-5.

The daytime T_g and amplitude decrease as the building height increases on both the summer and winter days, decreasing 42.81% and 34.71% for T_g from E2-1 to E2-5, respectively, due to the lower solar radiation reaching the ground. The sun elevation is low (30.92°) on winter day, and the ground is already covered by a large amount of shadows for building heights smaller than 30 m. As the building height

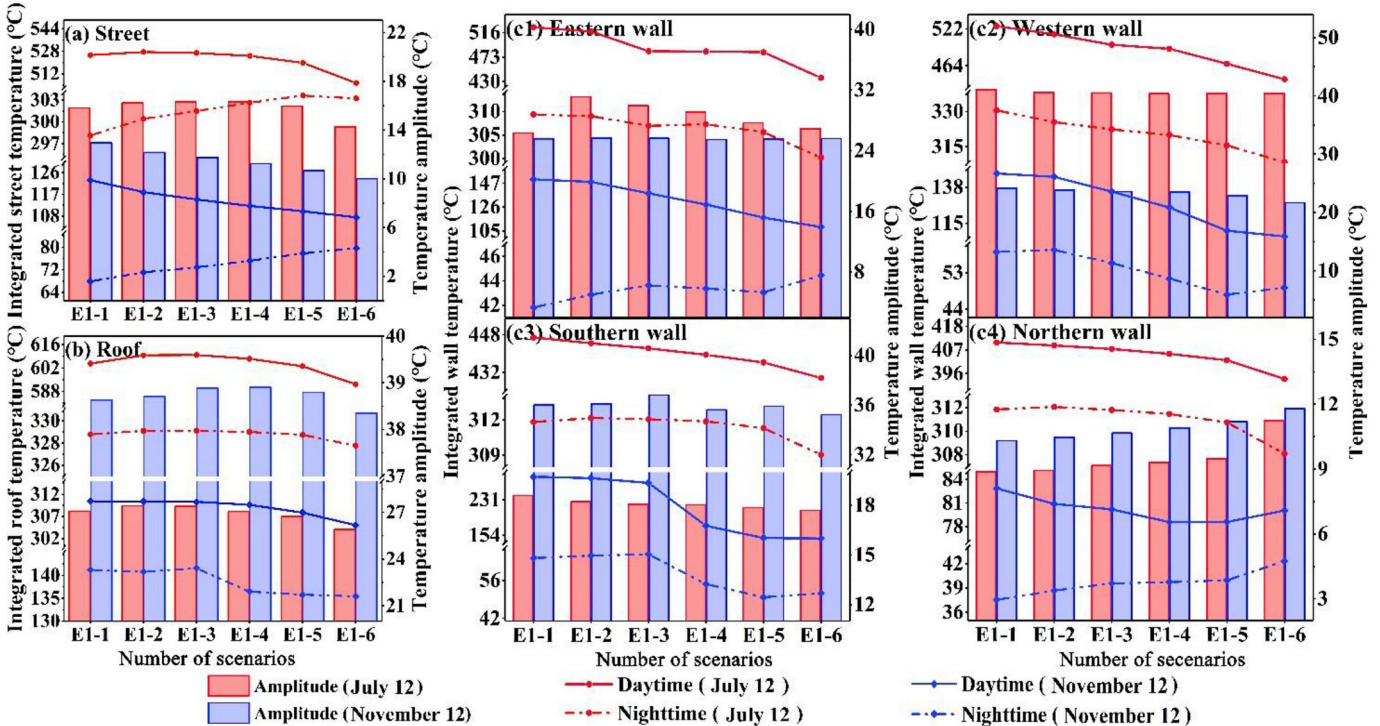


Fig. 4. Integrated surface temperature and amplitude with different building densities (λ_p) in the daytime and nighttime on July 12 and November 12, 2017. (a) Streets; (b) Roof; (c1)-(c4) four walls. The x-axis represents the building density changes from 0.0625 to 0.64.

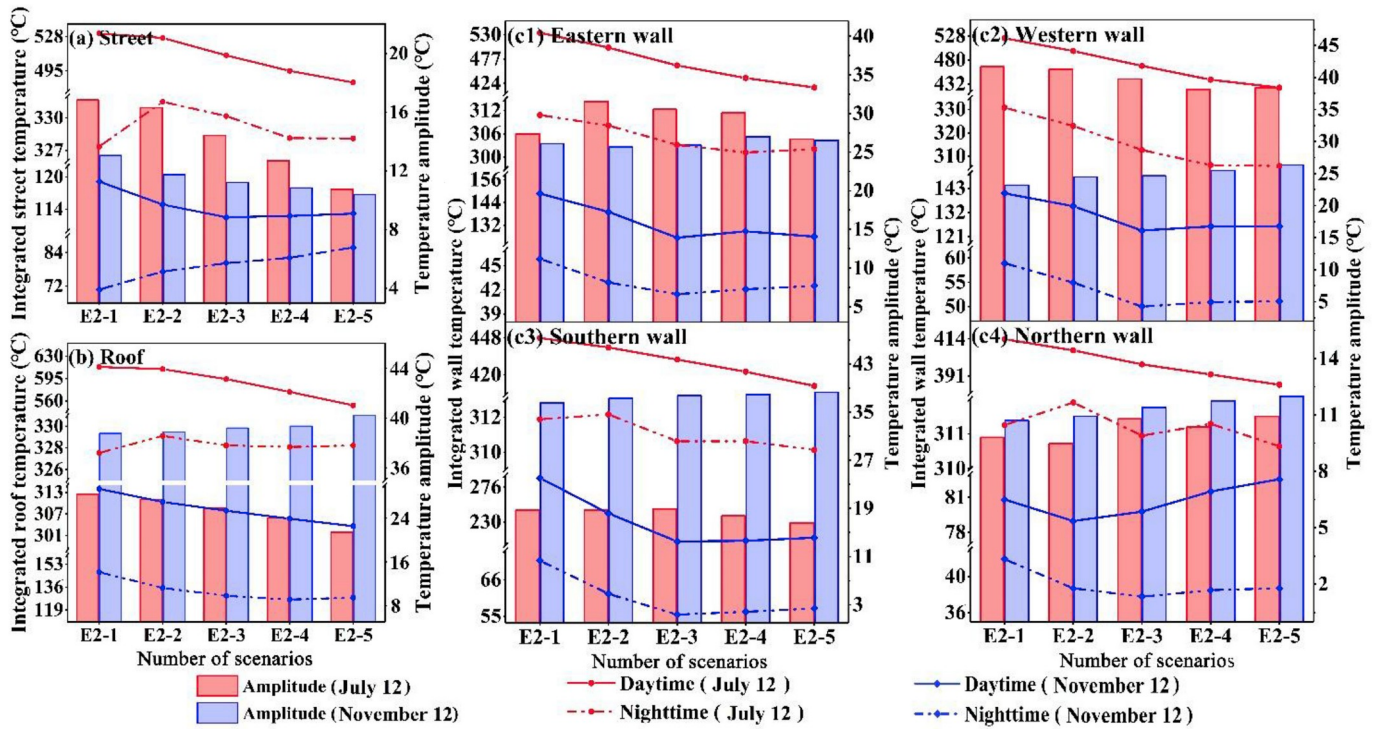


Fig. 5. Integrated surface temperature and amplitude with different building heights in the daytime and nighttime on July 12 and November 12, 2017. (a) Streets; (b) roof; (c1)-(c4) four walls. The x-axis represents the building height changes from 7.5 m to 60 m.

continues to increase, the variation in shadow area on the ground is small and has a slight influence on T_g , which produces an unchanged T_g with building height from E2-3 to E2-5. The stable and increased T_g at the summer and winter night respectively reveal that the block with lower buildings release more energy at night.

As the building height increases, T_e , T_w , T_s , and T_n decrease during the daytime on July 12. However, the variation in integrated temperature tends to be stable as the building height exceeds 30 m on November 12 except for the northern wall, which could be explained using the street analysis and the variations in wall shadow area on winter day are listed in Table 5 [37]. The nighttime T_e , T_w , and T_s variations for the two days that are consistent with the daytime variations indicate that the nighttime wall surface energy loss is mainly controlled by the daytime stored energy. The change in winter daytime and nighttime T_n are no more than 5 °C demonstrates that T_n is not sensitive to building height changes. For the four walls, weak-decreasing temperature amplitude trends occur on July 12 due to the decreased surface temperature caused by the increased wall shadows from E2-1 to E2-5, whereas weak-increasing temperature amplitude trends occur on November 12 might be controlled by the more severe temperature fluctuations because of the shadows on different building floors when the building height gradually increases.

With increasing building height, the daytime T_r decreases over the two days by the heat transfer between the lower-temperature walls and streets and the roof heat loss accelerated by the increased wind speeds

on the higher building floors [53]. These two reasons also apply to the amplitude variation on July 12 in Fig. 5, but the weaker change (rising 1.42 °C from E2-1 to E2-5) on November 12 reveals that the roof temperature amplitude is not sensitive to building height variations. The nighttime T_r keeps stable at a fixed FAR on summer day but has a similar trend with the daytime T_r on winter day.

4.3. The density and height combinations at a fixed FAR impact on the block surface temperature (FAR experiment)

Urban design should consider the block carrying capacity. In this section, we investigate the impacts of building height and density combinations on block surface temperatures at a fixed FAR and compare the results to the density and height experiments without controlling the FAR.

4.3.1. The FAR experiment results

The temperature distributions across street surfaces for the different building density and height combinations on July 12 and November 12 are listed in Table 6. The temperature distributions across the roof and wall surfaces are summarized in Table 7. Fig. 6 shows the T_g , T_e , T_w , T_s , T_n and T_r and their temperature amplitudes. The six building height and density combinations in Table 3 are E3-1, E3-2, E3-3, E3-4, E3-5 and E3-6.

The daytime T_g and amplitude on the summer day increase as the geometry combination changes from low-density and high-rise (E3-1) to medium-density and multistory (E3-4) combinations, but the variation tends to be stable for combinations with a higher building density and lower building height (E3-4 and E3-6). In the daytime on the winter day, the T_g and amplitude variations tend to be stable when the combination change from E3-1 to E3-4 but further decrease from E3-4 to E3-6. The reason might be that: (1) the inhibited energy loss from a relatively compact block on July 12 and smaller shadow areas produced by lower building heights cause the gradually increased daytime T_g from E3-1 to E3-4. The temperature increase caused by the more compact building geometry offsets the temperature decrease caused by the reduced

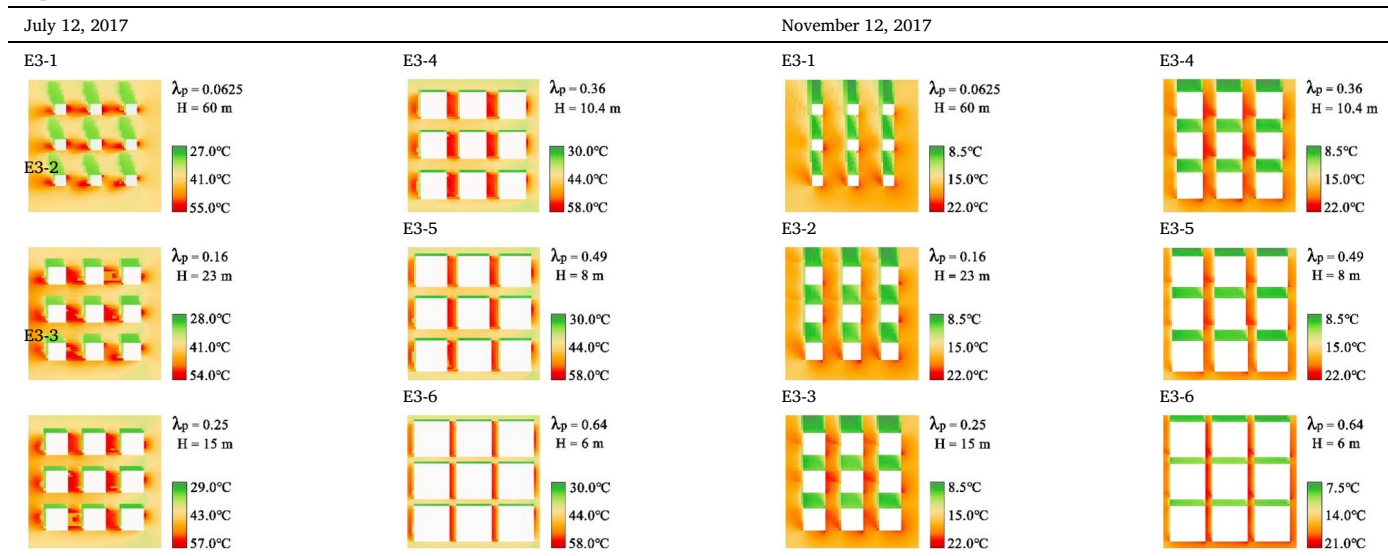
Table 5

The increases in daytime shadow area on the four walls from E2-1 to E2-5 on November 12, 2017.

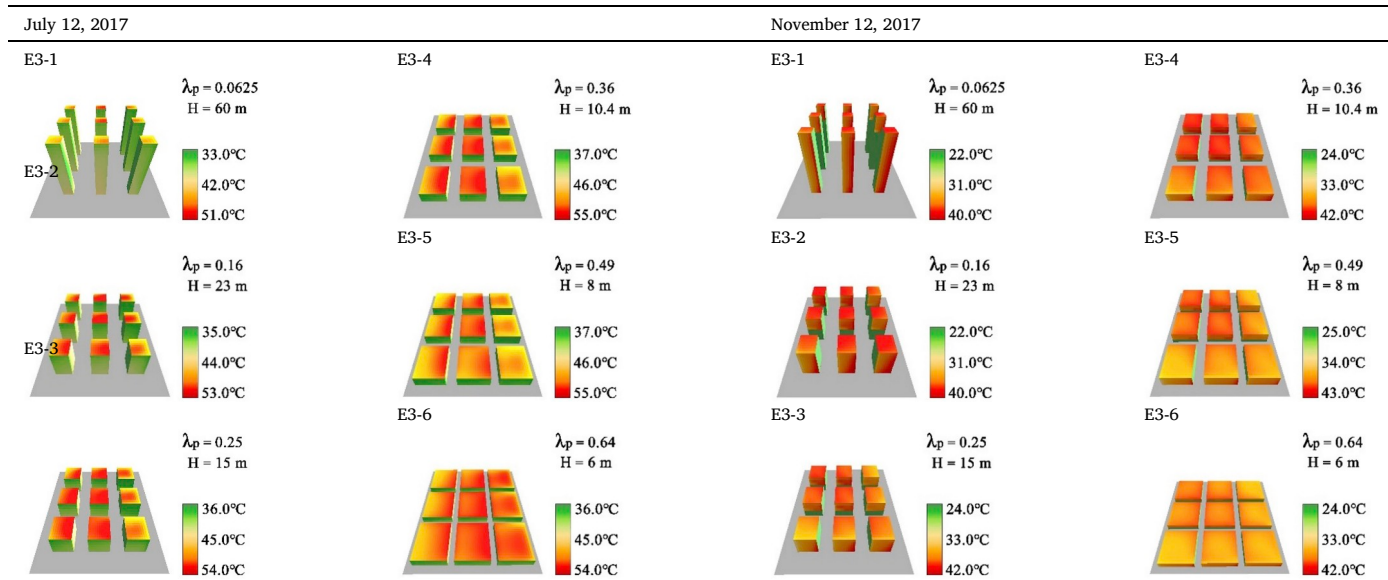
	Western wall (%)	Eastern wall (%)	Southern wall (%)	Northern wall (%)
from E2-1 to E2-3	11.37	14.35	32.60	5.19
from E2-3 to E2-5	3.05	3.43	5.43	0.13

Table 6

Simulated ENVI-met temperature distribution across street surfaces for the different building density and height combinations on summer and winter days. The temperatures were extracted from ENVI-met simulations at 12:00.

**Table 7**

Simulated ENVI-met temperature distributions across roof and wall surfaces for the different building density and height combinations on summer and winter days. The temperatures were extracted from ENVI-met simulations at 12:00.



radiation receiving areas on July 12 from E3-4 to E3-6, which results in an unchanged daytime T_g ; (2) The smaller daytime T_g variation from E3-1 to E3-4 on November 12 demonstrates that T_g is not sensitive to the building density when a large amount of building shadows cover the street, and it can be explained by the same reason of the summer daytime T_g variation from E3-4 to E3-6. The smaller nonshaded streets (see in Table 6) further decrease T_g from E3-4 to E3-6. On the other hand, the nighttime T_g shows a similar rising pattern over the two days, which demonstrates that a higher building density limits the heat loss from E3-1 to E3-6.

The daytime T_e , T_w , T_s and T_n variations from E3-1 to E3-6 on July 12 could be explained by the summer daytime T_g trend. The gradual reduction in building shadows caused by lower building heights and less solar radiation on the walls caused by higher building densities lead to the increase-decrease T_e , T_w , T_s and T_n trends, respectively, during the daytime on November 12, whereas T_n produces slight fluctuations

within 5 °C. The consistent nighttime T_e , T_w and T_s increases over the two days reveal that lower blocks with a higher building density at a fixed FAR could store more energy, but these temperature controlled by the daytime temperature become unchanged after E3-4 on July 12 and decrease after E3-5 on November 12. The chaotic but slight wall temperature amplitude variations (lower than 2 °C) demonstrate that temperature fluctuations would not become dramatic due to the stable energy received by the different-oriented walls over the two days in the case of controlling the FAR.

From E3-1 to E3-6, the daytime T_r show the same trends that first rising and then falling over the two days. The larger roof areas of the denser buildings receiving solar radiation might be the main reason for the T_r and temperature amplitude increases, while the inhibited T_r and amplitude increases from E3-4 to E3-6 on July 12 might be controlled by the accelerated heat transfer between roofs and four oriented walls with increasing received radiation differences between walls and roof from

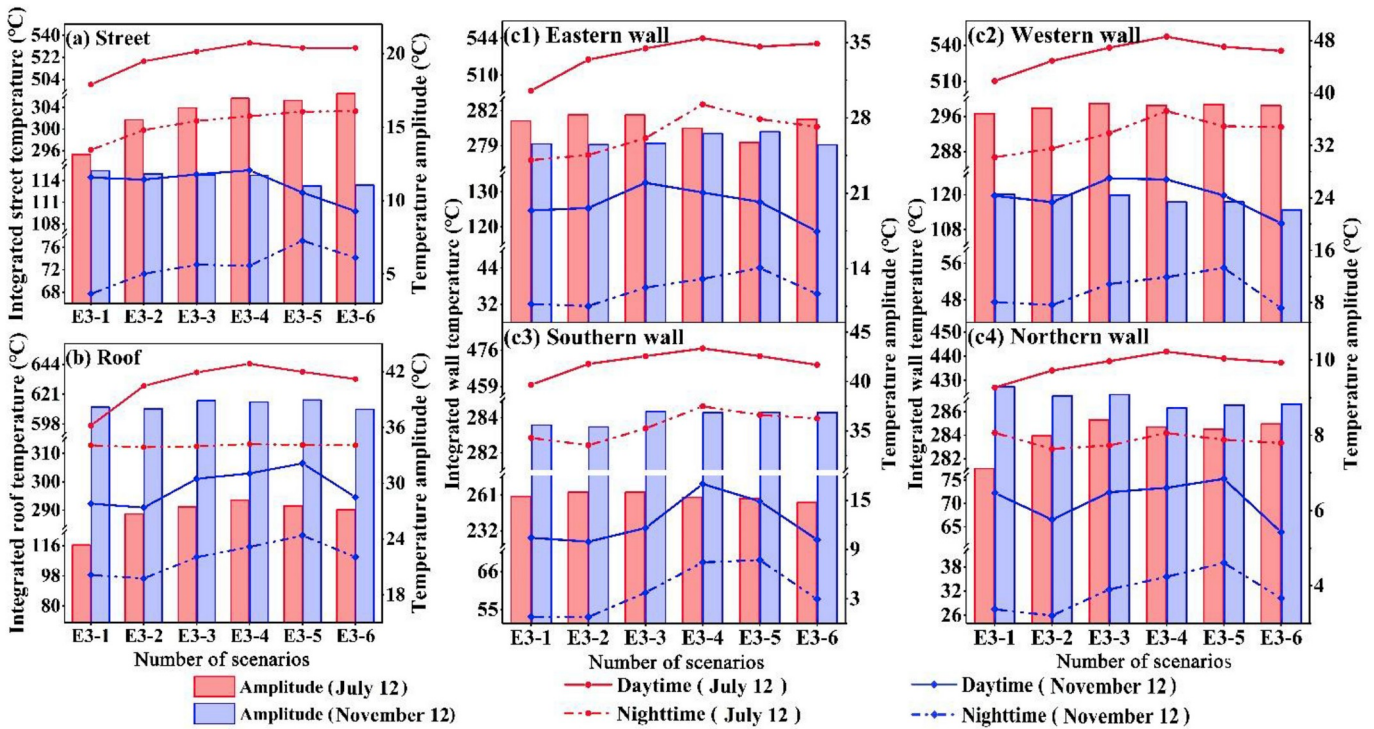


Fig. 6. Integrated daytime and nighttime surface temperatures and amplitudes with different building density and height combinations on July 12 and November 12, 2017. (a) Streets; (b) roof; (c1)-(c4) four walls. The x-axis represents different building height and density combinations with λ_p ranging from 0.0625 to 0.64 and H from 60 m to 6 m at a fixed floor area ratio (FAR).

E3-4 to E3-6 (**Table 8**). The same reason could be used to explain the decreased T_r from E3-5 to E3-6 on November 12, but the almost unchanged temperature amplitude on this day proves that the same solar radiation dominates the T_r stability from E3-1 to E3-6. The nighttime T_r trends over the two days keep consistent with that of height experiment.

4.3.2. Comparison of the density, height and FAR experiments

The influences of different building density and height combinations at a fixed FAR on block surface temperatures compared to single factor influences at unfixed FARs need to be thoroughly analyzed. In this section, we compared the integrated block surface temperature variations for the three experiments in the summer and winter daytime. In keeping with the building density and height changes from E3-1 to E3-6 in the FAR experiments in **Table 3**, the temperature trends in the density and height experiments are based on the density ranging from 0.0625 to 0.64 (from E1-1 to E1-6) and the height ranging from 60 m to 6 m (the block surface temperatures corresponding to the building heights in E3

were obtained by linear temperature interpolation from E2-1 to E2-5), respectively, and the comparison results are listed in **Table 9**. The λ_p and H values when the integrated surface temperature trends start changing in the FAR experiment would constitute the mutation point of the temperature variation trends. The temperature trends in the first and second stages in these three experiments based on the mutation points can be described by arrows. If the maximum temperature difference in every stage in these three experiments does not exceed 5 °C, this stage would be regarded as a stable state, otherwise the trend will be seen as increase or decrease.

For the integrated temperature variations, the coupling effects of the building density and height combinations show more complicated characteristics compared to those of the separate factors. The T_g trend on July 12 in E3 confirms that building height is the main factor controlling all T_g variations. In addition, building height and density are the decisive factors for the T_g variations in the first and second stages, respectively, on November 12. For the differently oriented walls, the building height effect is more significant in the first stage than the density but weaker in the second stage over the two days, except for the northern wall. The anomalous situation that occurs on the northern wall might because the daytime T_n caused by environmental radiance without direct solar energy is more complex and requires additional experiments to analyze. Similar to the other surfaces, the height is the dominant contributor to T_n in the first stage on summer and winter days, but the influence of density is not strong in the second stage over the two days.

From this section, we conclude that the building height mainly controls the integrated component surface temperature variations at lower densities and larger heights, indicating that the incident radiance variation caused by the mutual shadowing effect of buildings is the major driving factor. The density dominates the different integrated component surface temperatures at higher densities and lower heights demonstrating that preserved and released energy dominated by building intervals is an important contributor.

Table 8

The received radiance percentage of the different block surfaces from E3-1 to E3-6.

	July 12, 2017			November 12, 2017		
	Wall (%)	Roof (%)	Ground (%)	Wall (%)	Roof (%)	Ground (%)
E3-1	38.77	7.31	53.92	61.86	5.55	32.59
E3-2	27.01	19.90	53.09	46.24	17.57	36.19
E3-3	22.15	30.41	47.44	39.62	28.15	32.23
E3-4	17.48	42.09	40.43	32.92	39.99	27.09
E3-5	15.62	55.69	28.69	28.06	52.07	19.87
E3-6	12.78	68.58	18.63	21.40	64.98	13.62

Table 9

Comparison of the temperature variation trends in the three experiments with densities from 0.0625 to 0.64, heights from 60 m to 6 m and combinations from (0.0625, 60 m) to (0.64, 6 m).

	July 12, 2017				November 12, 2017			
	Mutation point	E1	E2	E3	Mutation point	E1	E2	E3
Street	$\lambda_p = 0.36$ H = 10 m	→\	/→	/→	$\lambda_p = 0.36$ H = 10 m	\→\	→→	→\
Eastern wall	$\lambda_p = 0.36$ H = 10 m	\→\	/↑	/\	$\lambda_p = 0.25$ H = 15 m	\→\	/↑	/\
Western wall	$\lambda_p = 0.36$ H = 10 m	\→\	/↑	/\	$\lambda_p = 0.25$ H = 15 m	\→\	/↑	/\
Southern wall	$\lambda_p = 0.36$ H = 10 m	\→\	/→	/\	$\lambda_p = 0.36$ H = 10 m	→\	/↑	/\
Northern wall	$\lambda_p = 0.36$ H = 10 m	\→\	/→	/\	$\lambda_p = 0.49$ H = 8 m	→→	→→	→\
Roof	$\lambda_p = 0.36$ H = 10 m	→\	/→	/\	$\lambda_p = 0.49$ H = 8 m	→→	/→	/\

5. Discussions

5.1. Temporal variations in component surface temperatures in the FAR experiment

Simply analyzing the mean integrated surface temperature ignores the temporal difference details between the six scenarios. In this section, the temporal changes in component surface temperature and the heterogeneity of temperature distribution over each component in the six scenarios are analyzed. Results in Fig. 7 show that for a specific component, the temperature heterogeneity increases as the mean surface temperature increases. Horizontal surfaces and vertical surfaces and walls of different orientations display different diurnal temperature patterns where the time at which the six components reach their maximum temperature is different dependent on the relative position of the surface normal vector and the sun direction. Streets, roofs and the

southern wall reach the maximum temperature at approximately 12:00 for summer and winter days when these surfaces receives more solar radiation. The temperature of the eastern and the western wall reaches the highest value in the morning and afternoon, respectively. The sun elevation is higher in winter than that in summer, so the southern wall absorbs more solar radiation on November 12 than on July 12. The maximum temperature of the northern wall is lower than that of other walls because the northern wall is shaded at most of time of a day. The FAR experiment in section 4.3.1 indicates that buildings with lower densities and larger heights could better cool blocks on July 12, but its cooling effect is not significant on November 12. From Fig. 7, the cooling effect is especially significant for the western wall where the temperature difference between other scenarios can be up to 10 °C at approximately 16:00 because higher buildings produce more shadows cooling the block surface. In addition, a sparser building geometry promotes heat conduction and accelerates heat loss. However, the difference of

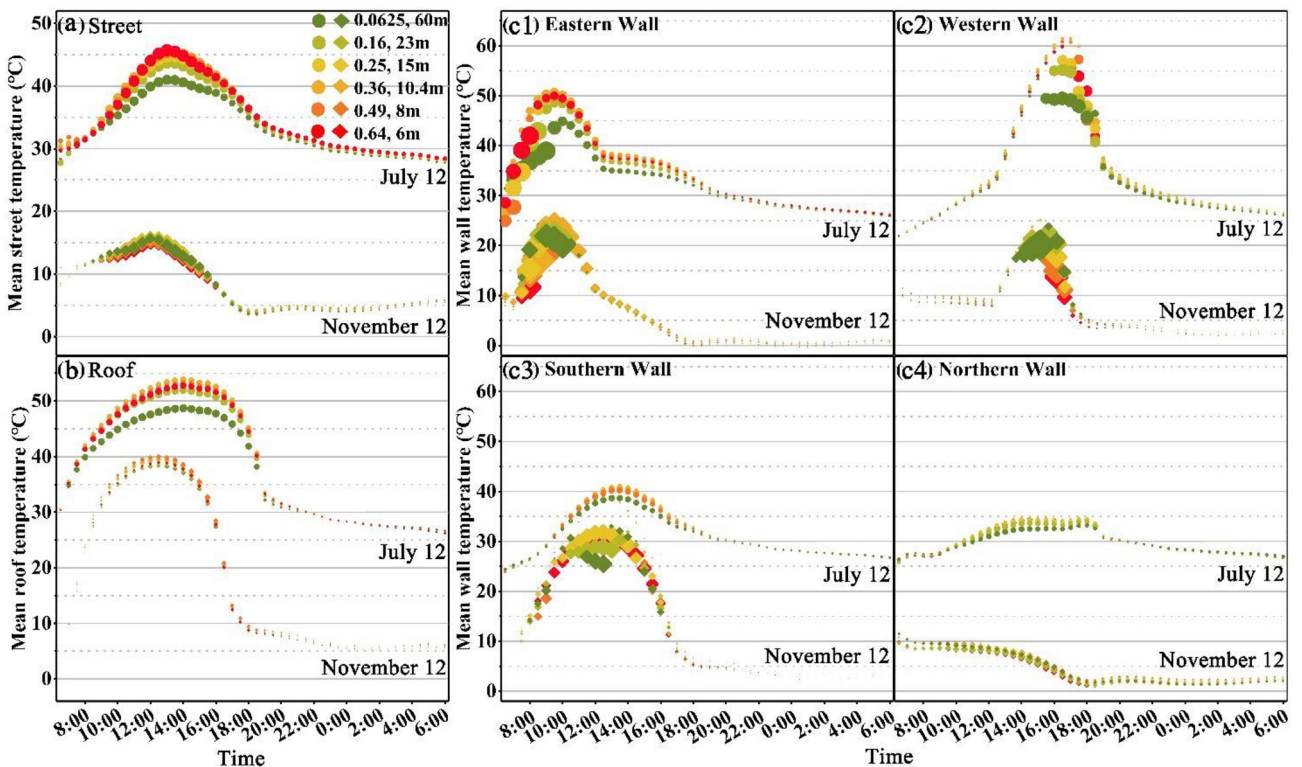


Fig. 7. Temporal difference in the component surface temperature for the different building density and height combinations on July 12 and November 12, 2017. (a) Streets; (b) roofs; (c1) - (c4) four walls. The circles and rhombuses are the temperatures on July 12 and November 12, 2017, respectively. The size of the points in each figure represents the temperature standard deviations of each component surface for nine buildings in every scenario in E3.

block temperature among six scenarios is smaller for November 12. For an example, the largest temperature difference between roofs in different scenarios is only 2 °C. More shadows could cover the southern wall with lower building density and larger building height due to the angle between the normal vector of the southern wall and the sun direction is smaller on November 12 than that on July 12. The larger shadow area percentages on the southern wall occur at noon in E3-1 and E3-2 when the sun elevation reaches highest (52.18%, 38.89% in E3-1 and E3-2 at 12:00, respectively). Therefore, the cooling effect of building shadows and a sparse building geometry produce sudden drops of the southern wall temperatures in E3-1 and E3-2 (see Fig. 7 (c3)).

Above results demonstrate that the temperature differences on July 12 between these six scenarios mainly occur when the temperature reach peak, but these scenario temperatures are similar on November 12 except for the southern wall.

5.2. The vertical heterogeneity of the wall surface temperature in E3-1 in the FAR experiment

The building geometry in E3-1 ($\lambda_p = 0.0625$, $H = 60$ m) could effectively cool blocks on a summer day, but the wall surface temperatures have vertical heterogeneities due to the different microclimate patterns of the different floors. Considering the ignored details of the mean wall surface temperature, the temporal temperature changes of the four walls for the different floors in E3-1 were extracted to analyze the temperature variations with different heights.

The temperature is lower in the lower part of the eastern and western walls in the morning (09:00) and afternoon (16:00), respectively because the sun is at a lower elevation and the shadows are cast on the lower part of walls by adjacent buildings. The temperature variation along height is smaller for November 12 because the sun elevation is smaller and shadows occupy a larger proportion on a specific wall compared to the summer case and the temperature difference between the sunlit and shaded parts is small as well. The temperature variation

along height at 13:30 displays an inverse pattern (decrease with building height) for the northern and southern walls on July 12 because the two walls receive less solar radiation but the lower floors receive more radiation emitted by the ground. For November 12, however, the temperature variation with height in the southern wall has an opposite trend to that of the northern wall which is attributed to the increased solar radiation reaching the higher parts of the southern wall and the increased mutual shadowing of buildings on lower floors of this wall when the sun elevation is low. Hence, solar radiation and ground-emitting radiation are the dominant contributors to the temperature heterogeneity on the eastern and western walls and the northern and southern wall, respectively for both the summer and winter case except for the southern wall on November 12 where the solar radiation is still the main driver. The eastern, western and southern walls receive solar radiation during a specific time period of a day. The sunlit and shaded status changes rapidly leading to a higher heterogeneity along height compared to the northern wall which can be seen from the error bars in Fig. 8.

The results show that vertical temperature heterogeneities always occur on the block surfaces. The lower floors of the eastern and western walls have lower surface temperatures on July 12 and November 12, but the opposite temperature variation along heights appears on the northern walls over these two days. In addition, the decreased sun elevation from summer to winter is an important cause of the seasonal differences of vertical temperature variation for the southern wall.

5.3. Limitations of this study

There are many problems that our current research cannot solve. (1) Considering that (a) the smaller modeling domains produce higher stability of simulation and shorter simulation duration and (b) all experiments could be ensured to compare in the same domains, the scenario designs in the three experiments in section 3.2 are based on 35 vertical grids and a vertical resolution of 3 m (the total domain height is

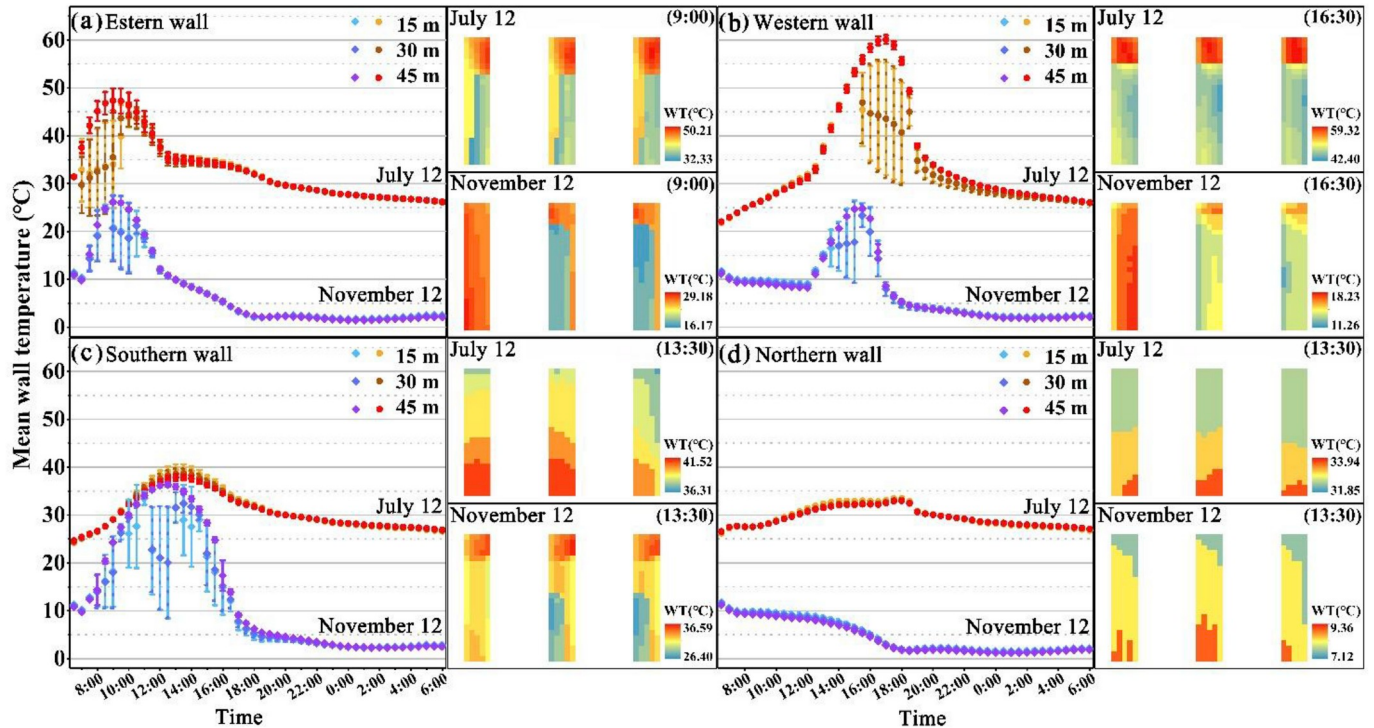


Fig. 8. Comparison of the temporal variation of wall temperature (WT) at different heights for the scenario $\lambda_p = 0.0625$, $H = 60$ m for July 12 and November 12, 2017. (a) Eastern wall; (b) western wall; (c) southern wall; and (d) northern wall. Error bar denotes the standard deviation of the temperature distribution over 9 buildings within a scene, and error bar on building floor of 30 m over the two days are represented by dotted lines due to the overlapping of the datasets (building floors of 15 m and 30 m).

105 m), but the scenarios of E2-5 ($\lambda_p = 0.25$, $H = 60$ m) and E3-1 ($\lambda_p = 0.0625$, $H = 60$ m) did not conform to the ENVI-met simulation rules that the domain height needs to exceed twice the height of the highest building [44]. Hence, two validation scenarios of E2-5 and E3-1 with 45 vertical grids (the total domain height is 135 m), called E2-5v and E3-1v, were constructed. The integrated block surface temperatures of E2-5v and E3-1v were compared with of E2-5 and E3-1 utilizing five statistics (R^2 , relative RMSE (rRMSE), relative MAE (rMAE), relative MBE (rMBE) and d), respectively, to evaluate the sensitivity of the surface temperature simulated by ENVI-met to the total domain height, and the results are listed in Fig. 9. The detailed statistical equations are provided in Table A1 in Appendix 1.

The rRMSE, rMAE and rMBE in the two experiments are not exceed $\pm 6\%$, especially close to 0 in the FAR experiment, but the larger statistics demonstrate that the height experiment is more sensitive to the total domain height than the FAR experiment in this study. The d values of approximately 0.8 and a significant difference (rRMSE, rMAE and rMBE) in the temperatures of E2-5 and E2-5v except for roof reveal that in the height experiment the summer nighttime surface temperature of ENVI-met simulation is more affected by the modeling domain height.

According to the statistics in the two comparisons, the influence of the modeling domain height on surface temperature simulation of ENVI-met is more significant in E2-5 than in E3-1, but cannot form conclusion only through these two scenarios and need more experiments to discuss, and the further studies will consider this issue.

(2) The influence of wind and vegetation in the blocks were not analyzed in our study, especially, the former reduces the solar energy reception of the block surfaces by accelerating heat transfer, and its contribution to the block surface temperature for different building heights, densities and combinations at a fixed FAR must be determined [54].

6. Conclusion

The 3-D urban microclimate simulation model ENVI-met was applied

to assess the building geometry impact on the block component surface temperature. The model accuracy in simulating component surface temperatures was validated using field data collected at the Fangshan Experiment Base. The assessment results show the following:

- (1) When the FAR is unfixed, decreasing the density for the medium-rise buildings ($H = 15$ m) and reducing the height for the medium density building ($\lambda_p = 0.25$) could produce higher block surface temperatures.
- (2) Compared to the independent building density and height changes at unfixed FARs, the variations in component surface temperature are more complicated in the different scenarios at a fixed FAR owing to the mutual density and height suppression influences. Increasing the density and decreasing the height result in general component surface temperature trends that first increase and then decrease on the summer and winter days. The building height is a dominant factor on component surface temperatures under lower-density and larger-height buildings on July 12 and November 12, while the density influence becomes stronger in the opposite situation.
- (3) Buildings with a density between 0.25 and 0.36 and a height between 8 m and 15 m at a fixed FAR have a better ability to increase the component surface temperatures on the summer and winter days. Moreover, a lower density ($\lambda_p = 0.0625$) and a larger building height ($H = 60$ m) constitute a relatively optimal environment to cool blocks on July 12 (approximate cooling effect of 5–10 °C). The similar temperature range between different building density and height combinations on November 12 makes the temperature on July 12 the primary consideration for block arrangement evaluation.
- (4) The temperature differences between different building floors can be up to 15 °C, demonstrating that the lower floors of high-rise buildings ($H = 60$ m) at a low density ($\lambda_p = 0.0625$) have cooler walls on July 12. Hence, the building geometry with a lower block surface temperature still has severe heterogeneities of component surface temperature in the vertical dimension.

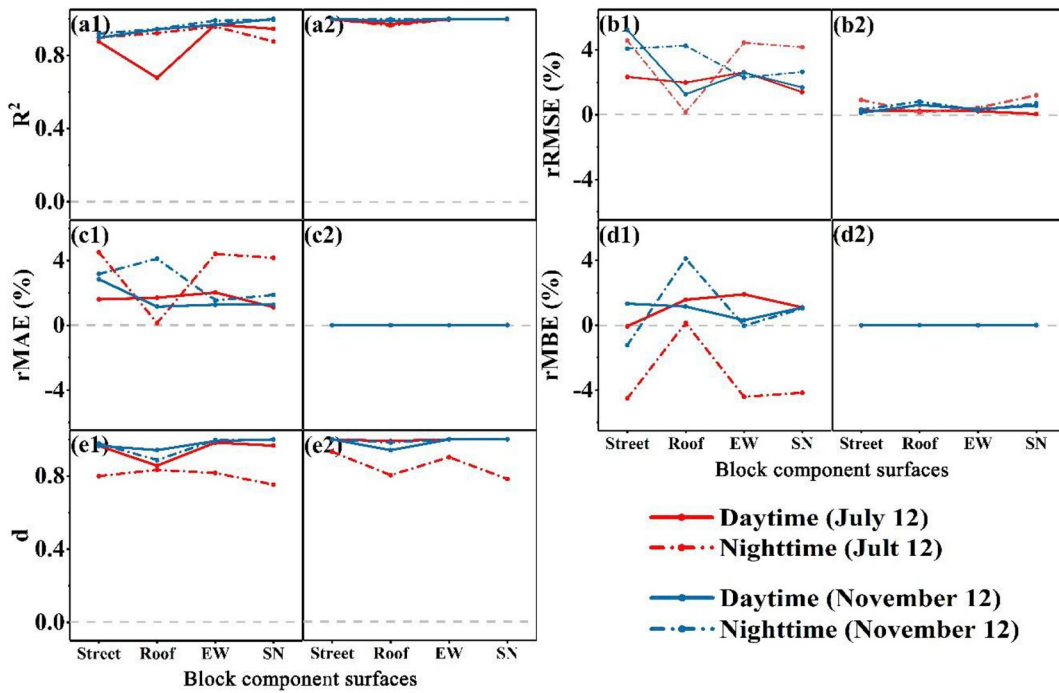


Fig. 9. Comparisons of block component surface temperature under different domain heights. (a1), (b1), (c1), (d1) and (e1) are the statistics for E2-5 and E2-5v; (a2), (b2), (c2), (d2) and (e2) are the statistics for E3-1 and E3-1v. EW, SN represent the average statistics of the eastern and western walls and of the southern and northern walls, respectively. The R^2 , rRMSE, rMAE, rMBE are indexes used to evaluate the difference between E2-5 and E2-5v, and E3-1 and E3-1v.

Declaration of competing interestCOI

The authors declare that they have no known competing financial interests or personal relationships that could have appeared to influence the work reported in this paper.

Acknowledgements

This work was supported by Beijing Natural Science Foundation

(8192025), National Natural Science Foundation of China (41771448 and 41571342), Science and Technology Plans of Ministry of Housing and Urban-Rural Development of the People's Republic of China and Opening Projects of Beijing Advanced Innovation Center for Future Urban Design, Beijing University of Civil Engineering and Architecture (UDC2019030821, UDC2017030212 and UDC201650100), Project of State Key Laboratory of Earth Surface Processes and Resource Ecology (2017-ZY-03), and in part by Beijing Laboratory of Water Resources Security.

Appendix A. Supplementary data

Supplementary data to this article can be found online at <https://doi.org/10.1016/j.buildenv.2019.106493>.

Appendix 1

Table A1
Details of nine statistics.

Statistics	Calculation formula [55]
std (Standard deviation)	$\text{std} = \sqrt{\frac{\sum_{i=1}^n (S_i - \bar{S})^2}{n-1}}$ or $\text{std} = \sqrt{\frac{\sum_{i=1}^n (M_i - \bar{M})^2}{n-1}}$
R ²	$R^2 = 1 - \frac{\sum_{i=1}^n (M_i - S_i)^2}{\sum_{i=1}^n (M_i - \bar{M})^2}$
RMSE (Root mean square error)	$\text{RMSE} = \sqrt{\frac{\sum_{i=1}^n (S_i - M_i)^2}{n-1}}$
rRMSE (Relative RMSE)	$\text{rRMSE} = \frac{\text{RMSE}}{S_i} \times 100\%$
MAE (Mean absolute error)	$\text{MAE} = \frac{\sum_{i=1}^n S_i - M_i }{n}$
rMAE (Relative MAE)	$\text{rMAE} = \frac{\text{MAE}}{S_i} \times 100\%$
MBE (Mean bias error)	$\text{MBE} = \frac{\sum_{i=1}^n (S_i - M_i)}{n}$
rMBE (Relative MBE)	$\text{rMBE} = \frac{\text{MBE}}{S_i} \times 100\%$
d (Index of agreement)	$d = 1 - \frac{\sum_{i=1}^n (S_i - M_i)^2}{\sum_{i=1}^n (S_i - \bar{M} + S_i - \bar{M})^2}$

Note: (1) S_i and M_i are the simulated value of ENVI-met and the measured value, respectively.
(2) In section 5.3, the S_i and M_i represent integrated component surface temperature values of the supplementary experiments (E2-5v and E3-1v) and scenario experiments (E2-5 and E3-1), respectively.

References

- Z.W. Yang, Y.B. Chen, Z.F. Wu, Q.L. Qian, Z.H. Zheng, Q.Y. Huang, Spatial heterogeneity of the thermal environment based on the urban expansion of natural cities using open data in Guangzhou, China, *Ecol. Indic.* 104 (2019) 524–534, <https://doi.org/10.1016/j.ecolind.2019.05.032>.
- S.L. Kingsley, M.N. Eliot, J. Gold, R.R. Vanderslice, G.A. Wellenius, Current and projected heat-related morbidity and mortality in Rhode Island, *Environ. Health Perspect.* 124 (4) (2016) 460–467, <https://doi.org/10.1289/ehp.1408826>.
- I.D. Stewart, T.R. Oke, Local climate zones for urban temperature studies, *B Am. Meteorol. Soc.* 93 (2012) 1879–1900, <https://doi.org/10.1175/BAMS-D-11-00019.1>.
- K. Deilami, M. Kamruzzaman, Y. Liu, Urban heat island effect: a systematic review of spatio-temporal factors, data, methods, and mitigation measures, *Int. J. Appl. Earth Obs.* 67 (2018) 30–42, <https://doi.org/10.1016/j.jag.2017.12.009>.
- B. Raji, M.J. Tenpierik, A.V.D. Dobbelsteen, The impact of greening systems on building energy performance: a literature review, *Renew. Sustain. Energy Rev.* 45 (2015) 610–623, <https://doi.org/10.1016/j.rser.2015.02.011>.
- C.B. Koc, P. Osmond, A. Peters, Evaluating the cooling effects of green infrastructure: a systematic review of methods, indicators and data sources, *Sol. Energy* 166 (2018) 486–508, <https://doi.org/10.1016/j.solener.2018.03.008>.
- M. Taleghani, Outdoor thermal comfort by different heat mitigation strategies-a review, *Renew. Sustain. Energy Rev.* 81 (2018) 2011–2018, <https://doi.org/10.1016/j.rser.2017.06.010>, 2018.
- E. Jamei, P. Rajagopalan, M. Seyedmohammadian, Y. Jamei, Review on the impact of urban geometry and pedestrian level greening on outdoor thermal comfort, *Renew. Sustain. Energy Rev.* 54 (2016) 1002–1017, <https://doi.org/10.1016/j.rser.2015.10.104>.
- J. Hang, M. Sandberg, Y.G. Li, J. Hang, Effect of urban morphology on wind condition in idealized city models, *Atmos. Environ.* 43 (4) (2009) 869–878, <https://doi.org/10.1016/j.atmosenv.2008.10.040>.
- A.J. Arnfield, Canyon geometry, the urban fabric and nocturnal cooling: a simulation approach, *Phys. Geogr.* 11 (3) (2013) 220–239, <https://doi.org/10.1080/02723646.1990.10642404>.
- Q.Y. Yi, X.S. Wang, G.Q. Zhang, H. Li, D. Janke, T. Amon, Assessing effects of wind speed and wind direction on discharge coefficient of sidewall opening in a dairy building model – a numerical study, *Comput. Electron. Agric.* 162 (2019) 235–245, <https://doi.org/10.1016/j.compag.2019.04.016>.
- S. Mirzaee, O. Ozgun, M. Ruth, K.C. Binita, Neighborhood-scale sky view factor variations with building density and height: a simulation approach and case study of Boston, *Urban Climate* 26 (2018) 95–108, <https://doi.org/10.1016/j.uclim.2018.08.012>.
- D.D. Wang, Y.H. Chen, Y.H. Cui, H. Sun, A geometric model to simulate urban thermal anisotropy for simplified neighborhoods, *IEEE T Geosci. Remote* 56 (2018) 4930–4944, <https://doi.org/10.1109/TGRS.2018.2842794>.
- K. Yu, Y.H. Chen, D.D. Wang, Z.X. Chen, A.D. Gong, J. Li, Study of the seasonal effect of building shadows on urban land surface temperatures based on remote sensing data, *Remote Sens.* 11 (2019) 497–522, <https://doi.org/10.3390/rs11050497>.
- J. Zhang, C.K. Heng, L.C. Malone-Lee, D.J.C. Hii, P. Janssen, K.S. Leung, B.K. Tan, Evaluating environmental implications of density: a comparative case study on the relationship between density, urban block typology and sky exposure, *Automat. Constr.* 22 (2012) 90–101, <https://doi.org/10.1016/j.autcon.2011.06.011>.

- [16] T. Sharmin, K. Steemers, A. Matzarakis, Microclimatic modelling in assessing the impact of urban geometry on urban thermal environment, *Sustain. Cities Soc.* 34 (2017) 293–308, <https://doi.org/10.1016/j.scs.2017.07.006>.
- [17] M.A. Bakarman, J.D. Chang, The influence of height/width ratio on urban heat island in hot-arid climates, *Procedia Eng.* 118 (2015) 101–108, <https://doi.org/10.1016/j.proeng.2015.08.408>.
- [18] E. Jamei, P. Rajagopalan, M. Seyedmahmoudian, Y. Jamei, Review on the impact of urban geometry and pedestrian level greening on outdoor thermal comfort, *Renew. Sustain. Energy Rev.* 54 (2016) 1002–1017, <https://doi.org/10.1016/j.rser.2015.10.104>.
- [19] A. Lai, M. Maing, E. Ng, Observational studies of mean radiant temperature across different outdoor spaces under shaded conditions in densely built environment, *Build. Environ.* 114 (2017) 397–409, <https://doi.org/10.1016/j.buildenv.2016.12.034>.
- [20] H. Sanaieian, M. Tenpierik, K.V.D. Linden, M.S. Fatemeh, M.S. Majid, Review of the impact of urban block form on thermal performance, solar access and ventilation, *Renew. Sustain. Energy Rev.* 38 (2014) 551–560, <https://doi.org/10.1016/j.rser.2014.06.007>.
- [21] H. Yan, S.X. Fan, C.X. Guo, F. Wu, N. Zhang, L. Dong, H. Yan, S. Fan, C. Guo, et al., Assessing the effects of landscape design parameters on intra-urban air temperature variability: the case of Beijing, China, *Build. Environ.* 76 (2014) 44–53, <https://doi.org/10.1016/j.buildenv.2014.03.007>.
- [22] F. Yang, F. Qian, S.S.Y. Lau, Urban form and density as indicators for summertime outdoor ventilation potential: a case study on high-rise housing in Shanghai, *Build. Environ.* 70 (2013) 122–137, <https://doi.org/10.1016/j.buildenv.2013.08.019>.
- [23] W.M. Shih, T.P. Lin, N.X. Tan, M.H. Liu, Long-term perceptions of outdoor thermal environments in an elementary school in a hot-humid climate, *Int. J. Biometeorol.* 61 (9) (2017) 1657–1666, <https://doi.org/10.1007/s00484-017-1345-x>.
- [24] C. Chatzipoulka, R. Compagnon, J. Kaempf, M. Nikolopoulou, Sky view factor as predictor of solar availability on building façades, *Sol. Energy* 170 (2018) 1026–1038, <https://doi.org/10.1016/j.solener.2018.06.028>.
- [25] A. Chatzidimitriou, S. Yannas, Street canyon design and improvement potential for urban open spaces: the influence of canyon aspect ratio and orientation on microclimate and outdoor comfort, *Sustain. Cities Soc.* 33 (2017) 85–101, <https://doi.org/10.1016/j.scs.2017.05.019>.
- [26] E. Andreou, Thermal comfort in outdoor spaces and urban canyon microclimate, *Renew. Energy* 55 (2013) 182–188, <https://doi.org/10.1016/j.renene.2012.12.040>.
- [27] A. Ghaffarianhoseini, U. Berardi, A. Ghaffarianhoseini, K. Al-Obaidi, Analyzing the thermal comfort conditions of outdoor spaces in an university campus in Kuala Lumpur, Malaysia, *Sci. Total Environ.* (2019), <https://doi.org/10.1016/j.scitotenv.2019.01.284>.
- [28] J.Y. Li, B.H. Zheng, W.Q. Shen, Y.F. Xiang, X. Chen, Z.Y. Qi, Cooling and energy-saving performance of different green wall design: a simulation study of a block, *Energies* 12 (2019) 15–32, <https://doi.org/10.3390/en12152912>.
- [29] H. Lee, J. Holst, H. Mayer, Modification of human-biometeorologically significant radiant flux densities by shading as local method to mitigate heat stress in summer within urban street canyons, *Adv. Meteorol.* 114 (2013) 6647–6662, <https://doi.org/10.1155/2013/312572>.
- [30] T.P. Lin, K.T. Tsai, R.L. Hwang, A. Matzarakis, Quantification of the effect of thermal indices and sky view factor on park attendance, *Landsc. Urban Plan.* 107 (2012) 137–146, <https://doi.org/10.1016/j.landurbplan.2012.05.011>.
- [31] K. Perini, A. Magliocco, Effects of vegetation, urban density, building height, and atmospheric conditions on local temperatures and thermal comfort, *Urban For. Urban Green.* 13 (3) (2014) 495–506, <https://doi.org/10.1016/j.ufug.2014.03.003>.
- [32] Q. Wang, Y. Li, J. Hang, L. Peng, The diurnal cycle of urban thermal environment in scale-model street canyons by outdoor field measurement, *Procedia Eng.* 198 (2017), <https://doi.org/10.1016/j.proeng.2017.07.126>, 7473–7757.
- [33] J. Zhang, Z.H. Gou, Y. Lu, P.Y. Lin, The impact of sky view factor on thermal environments in urban parks in a subtropical coastal city of Australia, *Urban For. Urban Green.* 44 (2019) 1–18, <https://doi.org/10.1016/j.ufug.2019.126422>.
- [34] I. Eliasson, Urban nocturnal temperatures, street geometry and land use, *Atmos. Environ.* 30 (3) (1996) 379–392, [https://doi.org/10.1016/1352-2310\(95\)00033-X](https://doi.org/10.1016/1352-2310(95)00033-X).
- [35] K. Niachou, I. Livada, M. Santamouris, Experimental study of temperature and airflow distribution inside an urban street canyon during hot summer weather conditions—Part I: air and surface temperatures, *Build. Environ.* 42 (8) (2008) 1383–1392, <https://doi.org/10.1016/j.buildenv.2007.01.039>.
- [36] H. Simon, J. Lindén, D. Hoffmann, P. Braun, M. Bruse, J. Esper, Modeling transpiration and leaf temperature of urban trees – a case study evaluating the microclimate model ENVI-met against measurement data, *Landsc. Urban Plan.* 174 (2018) 33–40, <https://doi.org/10.1016/j.landurbplan.2018.03.003>.
- [37] X.Y. Yang, Y.G. Li, The impact of building density and building height heterogeneity on average urban albedo and street surface temperature, *Build. Environ.* 90 (2015) 146–156, <https://doi.org/10.1016/j.buildenv.2015.03.037>.
- [38] Y. Topalar, B. Blocken, B. Maiheu, G.J.F.V. Heijst, A review on the CFD analysis of urban microclimate, *Renew. Sustain. Energy Rev.* 80 (2017) 1613–1640, <https://doi.org/10.1016/j.rser.2017.05.248>.
- [39] Beijing Municipal Commission of Planning and Natural Resources, Floor area index calculation rule, <http://ghrzzyw.beijing.gov.cn/>, 2006.
- [40] Beijing Municipal Commission of Planning and Natural Resources, Building engineering and area calculation specification, <http://ghrzzyw.beijing.gov.cn/>, 2005.
- [41] N. Antoniou, H. Montazeri, M. Neophytou, B. Blocken, CFD simulation of urban microclimate: validation using high-resolution field measurements, *Sci. Total Environ.* 695 (2019) 1–19, <https://doi.org/10.1016/j.scitotenv.2019.133743>.
- [42] J. Barr, J.P. Cohen, The floor area ratio gradient: New York City, 1890–2009, *Reg. Sci. Urban Econ.* 48 (3) (2014) 110–119, <https://doi.org/10.1016/j.regscurbeco.2014.03.004>.
- [43] M. Bruse, H. Fleer, Simulating surface–plant–air interactions inside urban environments with a three-dimensional numerical model, *Environ. Model. Softw.* 13 (1998) 373–384, [https://doi.org/10.1016/S1364-8152\(98\)00042-5](https://doi.org/10.1016/S1364-8152(98)00042-5).
- [44] P.J. Crank, D.J. Sailor, G. Ban-Weiss, M. Taleghani, Evaluating the ENVI-met microscale model for suitability in analysis of targeted urban heat mitigation strategies, *Urban Climate* 26 (2018) 188–197, <https://doi.org/10.1016/j.uclim.2018.09.002>.
- [45] S. Tsoka, A. Tsikaloudaki, T. Theodosiou, Analyzing the ENVI-met microclimate model's performance and assessing cool materials and urban vegetation applications—A review, *Sustain. Cities Soc.* 43 (2018) 55–76, <https://doi.org/10.1016/j.scs.2018.08.009>.
- [46] V.P. López-Cabeza, C. Galán-Marín, C. Rivera-Gómez, J. Roa-Fernández, Courtyard microclimate ENVI-met outputs deviation from the experimental data, *Build. Environ.* 144 (2018) 129–141, <https://doi.org/10.1016/j.buildenv.2018.08.013>.
- [47] F. Salata, L. Golasi, R.D.L. Vollaro, A.D.L. Vollaro, Urban microclimate and outdoor thermal comfort. A proper procedure to fit ENVI-met simulation outputs to experimental data, *Sustain. Cities Soc.* 26 (2016) 318–343, <https://doi.org/10.1016/j.scs.2016.07.005>.
- [48] K. Perini, A. Chokhachian, S. Dong, T. Auer, Modeling and simulating urban outdoor comfort: coupling ENVI-Met and TRNSYS by grasshopper, *Energy Build.* 152 (1) (2017) 373–384, <https://doi.org/10.1016/j.enbuild.2017.07.061>.
- [49] J.Y. Deng, N.H. Wong, X. Zheng, The study of the effects of building arrangement on microclimate and energy demand of CBD in nanjing, China, *Procedia Eng.* 169 (2017) 44–54, <https://doi.org/10.1016/j.proeng.2016.10.006>.
- [50] C.S. Gusson, D.H.S. Duarte, Effects of built density and urban morphology on urban microclimate calibration of the model ENVI-met V4 for the subtropical sao paulo, Brazil, *Procedia Eng.* 169 (2016) 2–10, <https://doi.org/10.1016/j.proeng.2016.10.001>.
- [51] L.H. Li, X.Q. Zheng, W.N. Xiang, Research on spatial distribution of building density in Beijing based on GIS, *Popul. Res. Environ. China* 18 (2008) 122–127, <https://doi.org/10.3969/j.issn.1002-2104.2008.01.024>.
- [52] R. Giridharan, S. Ganesan, S.S.Y. Lau, Daytime urban heat island effect in high-rise and high-density residential developments in Hong Kong, *Energ. Build.* 36 (2004) 525–534, <https://doi.org/10.1016/j.enbuild.2003.12.016>.
- [53] C.W. Kent, C.S.B. Grimmond, D. Gatey, J.F. Barlow, Assessing methods to extrapolate the vertical wind-speed profile from surface observations in a city centre during strong winds, *J. Wind Eng. Ind. Aerodyn.* 173 (2018) 100–111, <https://doi.org/10.1016/j.jweia.2017.09.007>.
- [54] Y.X. Xie, T.Y. Huang, J.N. Li, J.L. Liu, J.L. Niu, C.M. Mak, Z. Lin, Evaluation of a multi-nodal thermal regulation model for assessment of outdoor thermal comfort: sensitivity to wind speed and solar radiation, *Build. Environ.* 132 (2018) 45–56, <https://doi.org/10.1016/j.buildenv.2018.01.025>, 54.
- [55] C.J. Willmott, Some comments ON the evaluation OF model performance, *Phys. Geogr.* 2 (1982) 184–194, <https://doi.org/10.1080/02723646.1981.10642213>, 55.